

TOPICAL REVIEW • OPEN ACCESS

Recent progress on epitaxial growth of Fe-based superconducting thin films

To cite this article: Kazumasa Iida *et al* 2023 *Supercond. Sci. Technol.* **36** 063001

View the [article online](#) for updates and enhancements.

You may also like

- [Fe-based alloys and their shielding properties against directly and indirectly ionizing radiation by using FLUKA simulations](#)
M S Al-Buriah, D K Gaikwad, H H Hegazy et al.
- [Composition dependences and optimization of the magnetic properties of Fe-based metallic glasses](#)
Z Q Liu, M J Shi and T Zhang
- [Fe-based superconducting thin films—preparation and tuning of superconducting properties](#)
J Hänisch, K Iida, R Hühne et al.

Topical Review

Recent progress on epitaxial growth of Fe-based superconducting thin films

Kazumasa Iida^{1,6,*} , Jens Hänisch² , Satoshi Hata^{3,4,6} and Akiyasu Yamamoto^{5,6} 

¹ College of Industrial Technology, Nihon University, 1-2-1 Izumi-cho, Narashino, Chiba 275-8575 Japan

² Karlsruhe Institute of Technology, Institute for Technical Physics, Hermann-von-Helmholtz-Platz 1, D-76344 Eggenstein-Leopoldshafen, Germany

³ The Ultramicroscopy Research Center, Kyushu University, 744 Motoooka, Nishi, Fukuoka 819-0395, Japan

⁴ Interdisciplinary Graduate School of Engineering Sciences, Kyushu University, Kasuga, Fukuoka 816-8580, Japan

⁵ Department of Applied Physics, Tokyo University of Agriculture and Technology, 2-24-16 Naka-cho, Koganei-shi, Tokyo 184-8588, Japan

⁶ JST CREST, Kawaguchi, Saitama 332-0012, Japan

E-mail: iida.kazumasa@nihon-u.ac.jp

Received 1 January 2023, revised 20 March 2023

Accepted for publication 13 April 2023

Published 28 April 2023



CrossMark

Abstract

Since the discovery of Fe-based superconductors, a lot of effort has been devoted to growing single crystals and epitaxial thin films of them for fundamental studies and applied research of superconductivity. As a result, epitaxial thin films of the most of Fe-based superconductors have been realized. However, some of the materials, namely pristine and transition-metal-doped (Li,Fe)OHFeSe, hydrogen-doped $LnFeAsO$ ($Ln = Nd$ and Sm), Co-doped $SmFeAsO$, and K-doped $BaFe_2As_2$ have been available only in the form of single crystals due to, e.g. the difficulty in doping hydrogen, obtaining high-quality sintered bulks for the target used for pulsed laser deposition, and controlling volatile elements. By solving those issues, the aforementioned compounds have been successfully fabricated as epitaxial thin films in recent years. Unlike single crystals, transport critical current measurements are relatively easy on thin films, which can help evaluate the application potential. In this article, we give an overview over the growth methods for epitaxial thin films of those compounds, followed by their physical properties, especially focusing on electrical transport.

Keywords: Fe-based superconductors, epitaxial thin films, transport properties

(Some figures may appear in colour only in the online journal)

* Author to whom any correspondence should be addressed.



Original Content from this work may be used under the terms of the [Creative Commons Attribution 4.0 licence](https://creativecommons.org/licenses/by/4.0/). Any further distribution of this work must maintain attribution to the author(s) and the title of the work, journal citation and DOI.

1. Introduction

Whenever new functional materials are discovered, single crystals are immediately tried to be fabricated to understand their physical properties. Grain boundaries and impurities always mask the intrinsic physical properties. Therefore, such extrinsic factors should be eliminated as much as possible. To minimize the amount of impurities, a self-flux method (e.g. FeAs) has been commonly employed rather than low-melting solvents such as Sn for the growth of Fe-based superconductors.

However, single crystals are not always available, and even if the growth is possible, the available size is often extremely small and insufficient for bulk measurements. Epitaxial thin films sometimes offer the solution for such problems. Hydrogen-doped $LnFeAsO$ ($Ln = Nd$ and Sm), reviewed in this article, is a good example. In other cases, some of the materials have not been realized in the form of epitaxial thin films although single crystals have already been fabricated (K-doped $BaFe_2As_2$ and (Li,Fe)OHFeSe, both will be reviewed in this article). Hence, epitaxial thin films are complementary materials to single crystals for fundamental studies. Table 1 summarizes the chemical formula of the epitaxial thin films reviewed in this paper together with some references for films and single crystals.

Thin films are the preferable platform for certain investigations: optical measurements, particularly transmission, and the strain effect using the lattice and thermal expansion mismatch between films and substrates. Additionally, superlattices and monolayers that do not exist in nature can be fabricated, which opens a new opportunity to explore new functionalities.

In terms of applications, thin films are even necessary platforms. High-quality thin films are prerequisite for micro-electronic devices. Additionally, it is possible to evaluate the application potential especially for power applications by investigating the transport critical current properties.

In this review article, we focus on the Fe-based superconducting thin films that have appeared since 2017, namely (Li,Fe)OHFeSe, hydrogen-doped $LnFeAsO$ ($Ln = Nd$ and Sm), $SmFe_{1-x}Co_xAsO$ and K-doped $BaFe_2As_2$ in chronological order. A brief introduction of each compound will be presented, followed by the thin film growth and physical properties.

2. (Li, Fe)OHFeSe

2.1. Short introduction

Soft-chemical intercalation [26, 27] is a powerful tool for tailoring crystal symmetry and lattice parameters of functional materials. For FeSe, the nearly stoichiometric and most simple Fe-based superconductor, several intercalates have been investigated and found superconducting [28], such as alkali or earth-alkali elements (leading to deficient 122 type crystal structures), additional ammonia groups $(NH_3)_y$ or $(NH_2)_y(NH_3)_{1-y}$ [29], organic molecules

Table 1. The list of Fe-based superconductors reviewed in this article.

Chemical formula	Thin films	Single crystals
(Li,Fe)OHFeSe (including Mn doped samples)	[1, 2]	[3–7]
$LnFeAs(O,H)$ ($Ln = Nd$ and Sm)	[8–13]	[14]
$LnFe_{1-x}Co_xAsO$ ($Ln = La, Nd$ and Sm)	[15, 16]	[17–19]
$Ba_{1-x}K_xFe_2As_2$	[20–24]	[25]

(e.g. ethylenediamine) [30], tetrabutyl ammonium [31], cetyltrimethyl ammonium [32], and trimethylamine [33]), and LiOH [34] (for a review see, e.g. [6]). The latter leads to (Li,Fe)OHFeSe with superconducting transition temperature T_c of around 42 K and a crystal structure closely related to the $LnFeAsO$ structures of the pnictide Fe-based superconductors if the hydroxy group is regarded as single entity. It is so far the only intercalated Fe-based superconductor that has been successfully prepared in the form of thin films. Related compounds are (Li,Fe)OHFeS with lower T_c up to 8 K [35], hydrogen-free $LiFeO_2Fe_2Se_2$ (43 K) [36], and non-superconducting $(Na,Fe)OHFeCh$ ($Ch = Se, S$) [35].

The intercalation of the Fe-chalcogenide layers by ions or molecules leads to a stretching of the crystallographic c -axis, accompanied by an increase in T_c , where 42 or 43 K seems to be the maximum achievable in this system. These T_c values are also achievable on FeSe by applying pressure [37], or by direct charge carrier injection in electric double layer transistor experiments [38].

(Li,Fe)OHFeSe can be regarded as link between FeSe single crystals with T_c of 8 K and the FeSe unit cell films with T_c of 60 K, also regarding their two-dimensional (2D) nature and corresponding large crystallographic and electrical anisotropy. Like the unit cell films (and $A_xFe_{2-y}Se_2$, $A = K, Rb$; the 245 phase), its Fermi surface does not contain hole-pockets at the Γ point [5]. This is important because it shows that the missing hole-like-pockets are not due to interface effects, and that the existence of them is not necessarily a prerequisite for bulk superconductivity in Fe-based superconductors. (Li,Fe)OHFeSe shows different kinds of magnetic ordering, sometimes in coexistence with the superconducting phase [39, 40], re-emergent superconductivity at elevated pressures [41]; and even Majorana modes were recently detected [42]. It is therefore a very interesting platform for studying the mechanisms of superconductivity as well as the vortex matter in Fe-based materials. (Li,Fe)OHFeSe shares similarities with the highly anisotropic cuprates, foremost $Bi_2Sr_2Ca_{n-1}Cu_nO_{2n+4}$ ($n = 2$ or 3 , BSCCO) the material of 1st generation high- T_c superconducting wires and tapes: it shows strong 2D behavior, is relatively soft, and easily cleavable, and shows strong superconducting fluctuations and a large vortex liquid region. Compared to FeSe and other intercalated iron selenides, it is a rather clean system without problems of phase separation,

structural transitions, and interface effects. Its higher chemical stability in air compared to the monolayer FeSe renders it extremely useful for intrinsic-property measurements of the FeSe system.

2.2. Growth method

The growth of epitaxial, superconducting (Li,Fe)OHFeSe films was realized by Huang *et al* [1] and is based on the matrix-assisted hydrothermal growth (MHE) of (Li,Fe)OHFeSe single crystals [3]. A large $\text{K}_{0.8}\text{Fe}_{1.6}\text{Se}_2$ single crystal attached to a single crystal LaAlO_3 substrate is used as a seed or matrix for the crystalline film to grow in between. This is in contrast to other methods such as hydrothermal growth from commercial agents or hydrothermal intercalation of FeSe, which only produces polycrystalline samples. Degree of disorder as well as c -axis lattice constant and T_c are controllable by the growth parameters, such as temperature and time. Recently, transition-metal (TM)-doped films [43] and a sample series regarding the structural disorder [44] have been realized by the same group.

2.3. Physical properties

Huang *et al* showed in their first publications about (Li,Fe)OHFeSe films that T_c is correlated with c -axis lattice parameter (just as found for single crystals) as well as to the minimum in Hall resistance, i.e. the relative strength of the bands contributing to superconductivity [1]. The single crystalline films of extremely sharp texture showed high values of critical current density J_c (e.g. 0.5 MA cm^{-2} at $\sim 24 \text{ K}$ ($0.55T_c$) in zero field) despite their clean microstructure [45]. These films were studied in more detail shortly after [2] regarding the anisotropy of their electrical transport properties (similar unpublished data in figure 1). It was shown that (Li,Fe)OHFeSe films of optimal T_c are highly anisotropic (ratio of the upper critical fields for $H \parallel c$ and $\parallel ab$, $\gamma_{Hc2} = 11$ for temperatures sufficiently below T_c), nevertheless showing high pinning force densities F_p ($\sim 100 \text{ GN m}^{-3}$ at $4 \text{ K } H \parallel c$) and high self-field J_c values (extrapolated to 16 MA cm^{-2} at zero temperature). From this self-field J_c the penetration depth of (Li,Fe)OHFeSe was calculated to $\lambda \sim 160\text{--}200 \text{ nm}$ with the model of [46]. By analyzing the field orientation angle dependence of the exponent n of the $V(I)$ curves, intrinsic pinning at the layered crystal structure could be shown in nearly the complete temperature range.

Li *et al* were recently able to extend this research to TM-doped (Li,Fe)OHFeSe films [43]. Cu, Ni, Co, and Mn were tested as substitutes for Fe. They are homogeneously distributed and, according to neutron diffraction on Mn-doped deuterated single crystals [47], predominantly exchange the Fe in the (Li,Fe)OH layers. For all these substitutes, a T_c reduction of 0.5 K \%^{-1} was found, figure 2(a). This is in contrast to TM-doping of FeSe, where the maximum achievable T_c depends on the atomic radius of the TM element, and T_c is initially increased (except for Co, Cu, and Ni, which

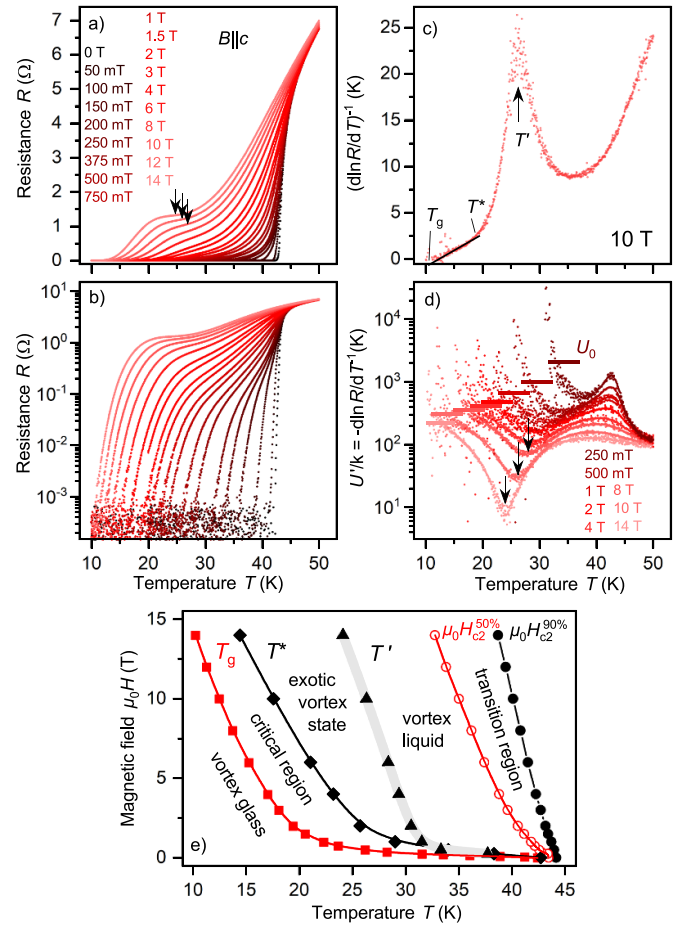


Figure 1. Resistive transition for fields $H \parallel c$ in linear (a) and logarithmic (b) presentation of a high-quality (Li,Fe)OHFeSe film (residual resistivity ratio, RRR = 64, sample A of [2]) together with the two logarithmic derivatives (c), (d) used for determining the characteristic temperatures glass-liquid transition T_g , critical region T^* , and exotic vortex phase transition T' (marked with arrows for the highest fields in (a), (c), (d)). The mean values of the activation energy U_0 determined from simple Arrhenius plots are marked by dashes in (d). (e) $H - T$ phase diagram.

leads to immediate T_c reduction of $\sim 3 \text{ K \%}^{-1}$) [48]. The same trends were found for Te-Te substitution: whereas T_c increases for $\text{FeSe}_{1-x}\text{Te}_x$ to a maximum of $\sim 15 \text{ K}$ in bulk samples, it decreases with $\sim 1 \text{ K \%}^{-1}$ in (Li,Fe)OHFeSe $_{1-x}\text{Te}_x$ [49]. This is probably simply due to the near optimum T_c of $42\text{--}43 \text{ K}$ of (Li,Fe)OHFeSe within the FeSe system. Especially Mn doping has been shown to be extremely beneficial for pinning and J_c , figure 2(b). In these films, pinning forces of $\sim 100 \text{ GN m}^{-3}$ have been measured at 5 K and 30 T , which is an increase by roughly a factor 10 compared to the pristine films [50] at this field or a shift of the F_p maximum of similar height from 4 T [2] to $\sim 35 \text{ T}$. The predominant pinning mechanism for both types of films was determined as normal surface pinning, where the (Li,Fe)OH interlayers were assumed to play a dominant role. The additional point-like disorder due to Mn ions within these sheets seems not to play a dominant role. Whether some kind of

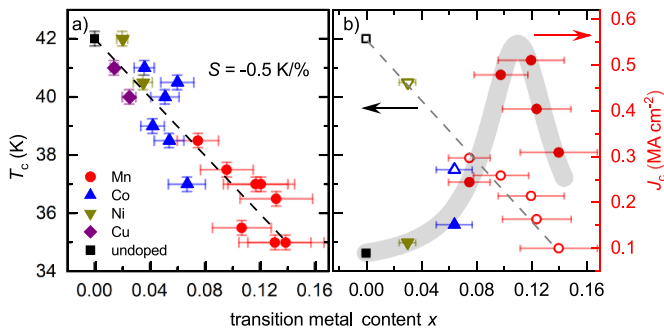


Figure 2. Effect of transition metal doping of (Li,Fe)OHFeSe thin films on (a) critical temperature T_c , and (b) critical current density J_c at 9 T and 10 K for $H \parallel c$. Reproduced from [43]. © IOP Publishing Ltd. All rights reserved.

magnetic interaction may contribute as well is still to be determined.

Clean samples of (Li,Fe)OHFeSe films, i.e. with high residual resistivity ratio (RRR) and near-optimum T_c values, show a distinct feature in their resistive transition for $H \parallel c$, see figure 1 (arrows) and [2, 44, 45], i.e. an extra hump near the irreversibility temperature. This feature is not due to inhomogeneities or grain boundary effects, since it develops with magnetic field and disappears for increased disorder by modified growth conditions [44] or TM doping [43]. In fact, it is the manifestation of a novel vortex phase within the vortex liquid, somehow related to but not equal to the vortex slush phase observed in $\text{YBa}_2\text{Cu}_3\text{O}_{7-\delta}$ (YBCO) films. The relationship to vortex phases in more 2D cuprates, such as BSCCO, is focus of recent investigations regarding transport anisotropy. Indeed, in a recent publication [51], Li *et al* showed that (Li,Fe)OHFeSe is equally anisotropic as BSCCO with H_{c2} anisotropies around 150 close to T_c with 2D-like angular dependence of H_{c2} , which allowed completing and explaining the vortex phase diagram within the vortex glass region. With the help of relaxation measurements and J_c maxima (determined via magnetization), the transition between a 3D vortex solid and quasi-2D pancake vortices was determined. This transition may easily explain the distinct features in $J_c(B)$ and $U_0(B)$ in [2] although at slightly higher fields for that particular sample. These results also indicate huge differences in the anisotropies of H_{c2} , ξ , and λ ; a distinct difference to the cuprates.

High-quality (Li,Fe)OHFeSe films facilitate the spectroscopy studies on the heavily electron-doped iron selenides. For example, the collective modes within superconducting gaps are identified from Raman spectra [52], emphasizing the Cooper pairing instabilities in the multi-band superconductors.

3. H-doped LnFeAsO ($\text{Ln} = \text{Nd}$ and Sm) and Co-doped SmFeAsO

3.1. Short introduction

LnFeAsO electron-doped by a partial substitution of oxygen with fluorine/hydrogen shows the highest superconducting

transition temperatures T_c among the Fe-based superconductors except for monolayers of FeSe. Hence, a lot of effort has been devoted to the growth of single crystals, however, the available size of those single crystals is typically around a few hundred μm^2 only. Recently, Kappenberger *et al* reported a new method to grow mm-sized single crystals of LaFeAsO [53] and $\text{LaFe}_{1-x}\text{Co}_x\text{AsO}$ [18, 19], which allows conducting bulk measurements (i.e. specific heat). However, such large crystals have not yet been reported for fluorine and hydrogen doped LnFeAsO (see e.g. [14]).

On the other hand, the thin film growth of LnFeAsO has also been started immediately in 2008 [54]. Unlike single crystals, epitaxial thin films of LaFeAs(O,F) [55] and NdFeAs(O,F) [56] have already been reported in 2010, followed by SmFeAs(O,F) [57] in 2011. The first superconducting F-doped LaFeAsO film was fabricated by a ‘solid-phase epitaxy’ method [58]. An amorphous precursor film was deposited at room temperature by pulsed laser deposition (PLD), followed by vacuum-sealing in a quartz tube together with a sintered LaFeAs(O,F) pellet. The whole arrangement was annealed at 960°C for 7 h. Microstructural analysis on the fully optimized LaFeAs(O,F) film revealed that a syntaxially grown La(O,F) layer was present between LaFeAs(O,F) and the LaAlO_3 substrate [59]. Besides, the LaFeAs(O,F) layer was covered with polycrystalline La(O,F) , which is an insulator and, therefore, should be removed for transport measurements.

To date, the parent compounds LnFeAsO ($\text{Ln} = \text{Nd}$ and Sm) have been readily fabricated by molecular beam epitaxy (MBE) and PLD [60, 61]. Additionally, epitaxial $\text{SmFe}_{1-x}\text{Co}_x\text{AsO}$ has been grown by PLD [15, 16]. For F doping, two methods, namely one-step and two-step growth, have been reported. For the former method [62, 63], however, the reproducibility is not good. One of the reasons is the fluorine source such as FeF_3 , which is highly hygroscopic. As a result, HF rather than F gas was supplied during the growth. Nevertheless, a high T_c of 55 K was achieved for SmFeAs(O,F) [64].

On the other hand, the latter method for F-doping has shown high reproducibility. After growth of parent LnFeAsO , a LnF over-layer was deposited. During deposition, F diffused into LnFeAsO , resulting in superconducting LnFeAs(O,F) . The structural characterization by x-ray diffraction revealed that LnF turned into insulating Ln(O,F) . Interestingly, Ln(O,F) grows epitaxially on LnFeAs(O,F) with $(001)[110]\text{Ln(O,F)} \parallel (001)[100]\text{LnFeAs(O,F)}$. Fortunately, the LnFeAs(O,F) film is not fully covered with insulating Ln(O,F) , which makes transport measurements even without removal of Ln(O,F) possible.

Unlike fluorine doping, hydrogen-doped LnFeAsO was obtained only by a post-growth process. The distinct difference between F and H is their solubility limit. The upper limit of the former for SmFeAsO is around 20% [65], whereas of the latter is up to 80% [66]. Hence, it is possible to explore the physical properties of heavily electron-doped LnFeAsO . Another feature is that no over-layers had to be formed on LnFeAs(O,H) , which is highly beneficial especially for fabricating bi-layer structures.

3.2. Growth methods

3.2.1. Pulsed laser deposition, PLD. For PLD, a second-harmonic Nd:YAG laser (wave length of 532 nm) has been selected rather than an excimer laser, since the *in-situ* phase formation has been realized only by Nd:YAG laser so far. The deposition process was conducted under a base pressure of 1×10^{-6} Pa. The phase-pure PLD target was ablated with a repetition rate of 10 Hz. Importantly, impurity phases from the target should be eliminated as much as possible, especially Ln_2O_3 and $Ln(O,F)$ [54]. Both LaFeAsO [54] and SmFeAsO [61] were epitaxially grown on MgO (001) and $(LaAlO_3)_{0.7}(Sr_2TaAlO_6)_{0.7}$ (001) [LSAT (001)]. Similarly, $SmFe_{1-x}Co_xAsO$ epitaxial thin films were realized on various substrates using almost the same deposition setup [15, 16]. For phase purity and epitaxy, the optimum deposition temperature and substrate were 860 °C and MgO, although a small amount of Sm_2O_3 was present. However, the films grown on MgO have not shown superconductivity, in contrast to the films on $LaAlO_3$ and $MgAl_2O_4$, which showed onset of superconductivity, yet more foreign phases. It was concluded, that strain effects on MgO suppressed superconductivity. Only the film grown on $CaF_2(001)$ showed zero resistance at 8.2 K [15]. In this case, cobalt and fluorine co-doping may occur. Later, growth on MgO buffered with Co-doped $BaFe_2As_2$ yielded a T_c of 13–18 K for $SmFe_{1-x}Co_xAsO$ [16]. Unfortunately, J_c measurements have not been reported so far.

3.2.2. Molecular beam epitaxy, MBE. As stated above, parent compound NdFeAsO epitaxial thin films have been readily fabricated [60], although small tuning is always necessary due to slight change in the growth chamber condition over time (e.g. pressure of the deposition chamber). Nevertheless, the deposition method is briefly described. Solid sources of NdF_3 , Fe, As, Fe_2O_3 , and Ga were charged in Knudsen cells. Oxygen was provided via thermal decomposition of Fe_2O_3 . Ga has been used to remove excess fluorine during deposition. Although fine tuning is necessary, parent compound NdFeAsO has been fabricated on a large variety of oxide and fluorine substrates [67], as well as technical substrates [68, 69]. Typical growth temperatures are around 800 °C. The growth rate is approximately $0.8\text{--}1\text{ nm min}^{-1}$. Most of these films were grown for 30 min, resulting in 24–30 nm thickness.

3.2.3. Topotactic reaction using AeH_2 ($Ae = Mg, Ca, Sr$ and Ba). Initial attempts for hydrogen doping of epitaxial films have been made by flowing H_2 or H-radical gases during deposition [54]. However, none of them were successful. In 2019, the topotactic chemical reaction using CaH_2 for SmFeAs(O,H) was reported [8], followed by NdFeAs(O,H) [11]. The reagent powder CaH_2 is in physical contact with the films, which is the key to promote the reaction with homogeneous distribution of H. Any AeH_2 ($Ae = Mg, Ca, Sr$ and Ba) can be used as hydrogen source [9]. Although the desorption temperature of AeH_2 is Ae -dependent, the optimized temperature for the topotactic reaction is around 500 °C except for $Ae = Mg$, which requires only 380 °C.

To obtain reliable results, storing and handling of the CaH_2 powder should be conducted in a controlled Ar-glove box, since CaH_2 easily absorbs moisture and turns into $Ca(OH)_2$ and H_2 gas. This leads to a change in the amount of CaH_2 consumed during the topotactic reaction. A schematic illustration of the procedure is shown in figure 3. The process temperature should be less than 520 °C, otherwise, the quartz tube will rupture by increased inner pressure during heat treatment.

Quantitative analysis of H content has already been conducted using secondary ion mass spectroscopy (SIMS) with a $SmFeAsO_{0.4}H_{0.6}$ bulk polycrystalline sample as [8]. The depth profile by SIMS for the SmFeAs(O,H) thin film showed inhomogeneous doping of H. The H content with respect to oxygen decreased from 0.34 at the surface to 0.1 at the film/substrate interface. An effective method to avoid such inhomogeneous H doping is decreasing the film thickness, which was proved by the microstructural analysis by transmission electron microanalysis (TEM), shown in figure 4 [12]. The 24 nm thick NdFeAs(O,H) film is microstructurally clean (figure 4(a)). The averaged c -axis length determined by the image intensity profile for the H-doped NdFeAsO near the film/substrate interface was almost the same as near the film surface and smaller than that for the parent NdFeAsO. As the c -axis length is decreased with H-doping compared with the parent compound [8], hydrogen was concluded to be partially and homogeneously substituted for oxygen in NdFeAsO.

The effective carrier number per O (x_{film}) is estimated as $1/e|R_H| \times V/2$, where e is the charge of the carrier, R_H is the Hall coefficient measured at 50 K, and V is the unit cell volume evaluated by x-ray diffraction. The carrier density was estimated with the single-carrier model. The Hall coefficient was negative for all samples, and thus the dominant carriers are electrons. Figure 5 shows the x_{film} dependence of T_c for various NdFeAs(O,H) films. For comparison, the data of NdFeAs(O,F) are also shown in the same graph. The maximum x_{film} for the F-doped films was around 0.15, whereas the corresponding value for H-doping was 0.5. Hence, the maximum electron concentration for NdFeAs(O,H) is higher than that for NdFeAs(O,F). T_c is constant for a wide range of x_{film} , which is similar to bulk polycrystalline samples. This gives a good opportunity to investigate how heavy electron doping affects the superconducting properties, which will be discussed in the following sub-section.

3.2.4. Physical properties of SmFeAs(O,H). $SmFeAsO_{1-x}H_x$ with $x \sim 0.35$ showed an onset T_c of around 48 K [8]. CaH_2 was used for the topotactic chemical reaction. The anisotropy value estimated from the ratio of the upper critical fields for $H \parallel ab$ and $\parallel c$ near T_c was 2.4. To date, no transport J_c has been reported, but magnetic J_c was measured for SmFeAs(O,H) fabricated by different hydrogen sources, AeH_2 ($Ae = Mg, Ca, Sr$ and Ba). Among them, MgH_2 showed the lowest desorption temperature (<400 °C), and hence the optimum processing temperature for the topotactic transformation was the lowest (~ 380 °C). This may explain

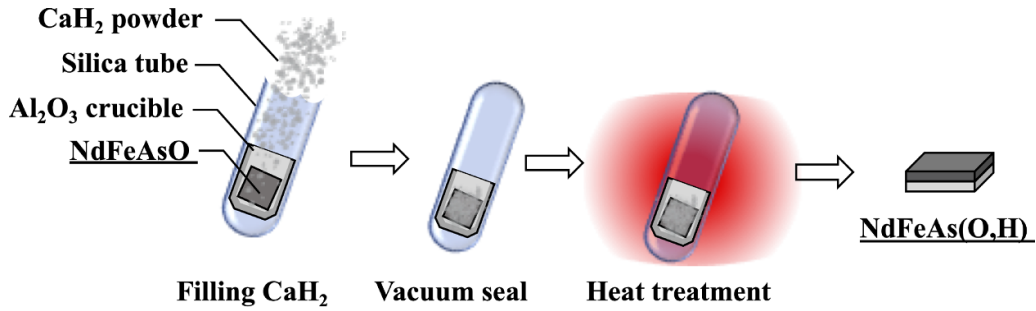


Figure 3. Schematic illustration of the topotactic reaction.

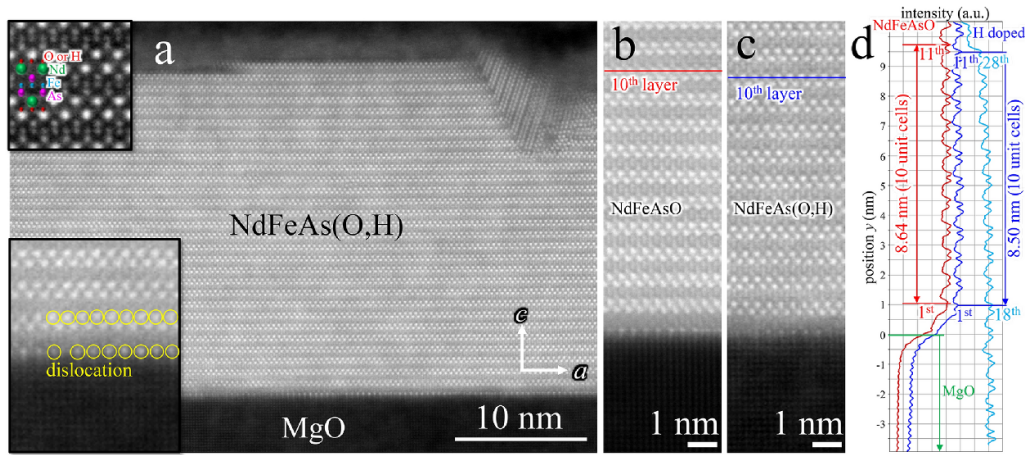


Figure 4. Microstructural analysis by TEM. (a) TEM cross-sectional view of the NdFeAs(O,H) epitaxial thin film revealed almost no apparent defects. Additionally, no reaction layer between the film and the MgO substrate was observed. (b) The magnified ADF images of NdFeAsO and (c) NdFeAs(O,H). (d) Image intensity profiles along the c -axis direction extracted from (b) and (c), averaged in the a -axis direction. The c -axis lattice parameters averaged over 10 layers are 8.64 Å and 8.50 Å, respectively. The distances from the 1st to the 11th layer and from the 18th to the 28th layer are the same in the NdFeAs(O,H) film. Reproduced from [12]. CC BY 4.0.

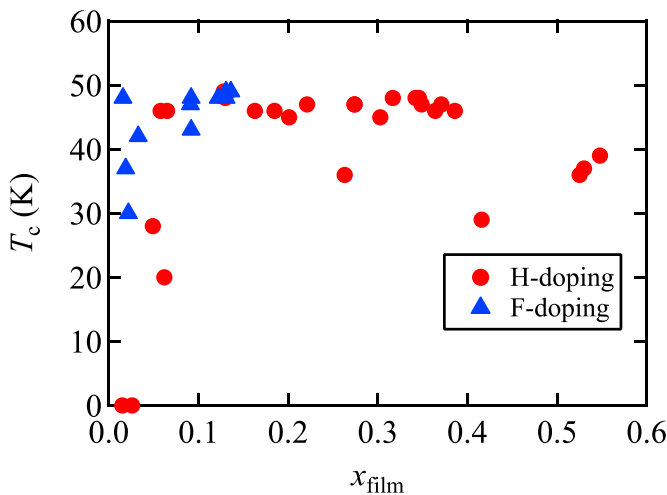


Figure 5. The superconducting transition temperature (T_c) as a function of the effective carrier number per O (x_{film}) for NdFeAs(O,F) and NdFeAs(O,H) films. The carrier density at 50 K was estimated with the single-carrier model.

the low T_c values for SmFeAs(O,H) ($T_{c,\text{onset}} = 20.5$ K and $T_{c,\text{zero}} = 13.5$ K). On the other hand, all SmFeAs(O,H) fabricated with AeH_2 other than MgH_2 showed an onset T_c over

40 K, where SmFeAs(O,H) via BaH_2 exhibited the highest T_c ($T_{c,\text{onset}} = 49$ K and $T_{c,\text{zero}} = 44.4$ K). A self-field J_c of 2 MA cm^{-2} was recorded at 2 K, which is almost the same as for F-doped SmFeAsO [57].

Recently, the upper critical fields H_{c2} of SmFeAs(O,H) have been experimentally determined in pulsed fields up to 130 T [10]. An H_{c2} of 120 T was measured at 2.2 K for $H \parallel ab$. For $H \parallel c$, H_{c2} was estimated to be around 80 T at zero kelvin using a dirty-limit two-band model. Angular dependence of H_{c2} at 37.5 K revealed that the anisotropy was around 2.

3.2.5. Physical properties of NdFeAs(O,H). Relatively homogeneous H-doping was achieved for NdFeAs(O,H) by reducing the film thickness as stated above. Figure 6(a) compares the temperature dependence of resistivity for NdFeAs(O,H) with a NdFeAs(O,F) film on the same type of MgO substrates. H-doping was conducted using CaH_2 at 520°C for 36 h. The calculated x_{film} was around 0.22. Although T_c around 45 K was almost the same for both F- and H-doped NdFeAsO, the normal state resistivity for NdFeAs(O,H) was lower than that for NdFeAs(O,F). This is mainly due to the larger amount of electron doping for NdFeAs(O,H).

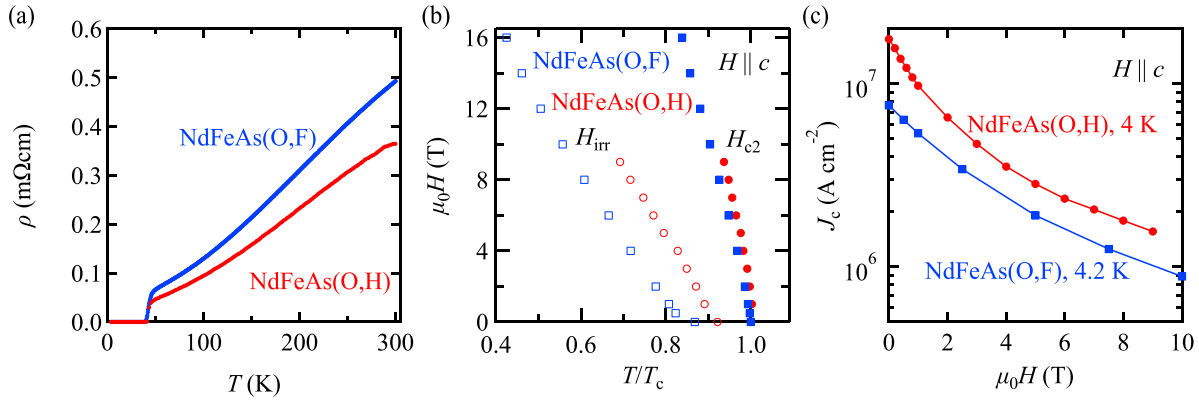


Figure 6. Comparison of the physical properties between NdFeAs(O,H) and NdFeAs(O,F). (a) Temperature dependence of the resistivity. (b) The upper critical field H_{c2} and the irreversibility field H_{irr} for $H \parallel c$ as a function of reduced temperature. (c) Low-temperature field dependence of J_c for $H \parallel c$. The data were re-produced from [11, 17].

As in [11], the anisotropy γ of the upper critical field H_{c2} of NdFeAs(O,H) was lower than that of NdFeAs(O,F) ($\gamma = 4.5$ versus 5.1). A low anisotropy was observed not only in the superconducting state but also in the normal state for NdFeAs(O,H) [13]. According to the band calculation for CaFeAsH and CaFeAsF (both have the same crystal structure of ZrCuSiAs type) by Muraba *et al*, the former showed a more three-dimensional character of the Fermi surface compared to the latter [70]. Similar to CaFeAsH, the lower anisotropy of NdFeAs(O,H) may be due to the more three-dimensional character of the Fermi surface.

The irreversibility field H_{irr} for $H \parallel c$ is related to H_{c2} by the following formula: $H_{irr} \propto \gamma^{-2} H_{c2}$ [72]. Hence the smaller anisotropy, typically the bigger H_{irr} at a given (reduced) temperature for a certain system. In fact, H_{irr} for NdFeAs(O,H) is larger than that for NdFeAs(O,F) (figure 6(b)), whereas H_{c2} of NdFeAs(O,H) is comparable to that of NdFeAs(O,F).

Heavy electron doping benefits not only low anisotropy but also high critical current density. Figure 6(c) shows the field dependence of transport J_c at 4 K. Magnetic field was applied parallel to the crystallographic c -axis. As can be seen, self-field J_c reached over 17 MA cm^{-2} at 4 K. This value is more than twice the best-performing NdFeAs(O,F) film having an onset T_c of 45 K [71]. Since the film is microstructurally clean (figure 4(a)), J_c decreased rather quickly with field. As discussed in [12], the high J_c may be due to the short penetration depth λ by heavy electron doping, although the direct evidence is still missing. Recently, considerable improvement of J_c by over-doping has been reported for $\text{YBa}_2\text{Cu}_3\text{O}_y$ [73]. Stangl *et al* concluded that the condensation energy was increased by over-doping. Furthermore, by combining a thermodynamic approach with microstructural modification by BaHfO₃ nano particles, Miura *et al* reported on a record pinning force density F_p of 3.17 TNm^{-3} at 4.2 K and 18 T ($H \parallel c$) for $(\text{Y,Gd})\text{Ba}_2\text{Cu}_3\text{O}_{7-\delta}$ grown on technical substrate [74]. As shown in figure 5, T_c is almost constant in a wide range of doping for NdFeAs(O,H), which is the most suitable system for the improvement of J_c by heavy carrier doping.

4. $\text{Ba}_{1-x}\text{K}_x\text{Fe}_2\text{As}_2$

4.1. Short introduction

Unlike electron and isovalently doped BaFe_2As_2 (Ba122), the epitaxial growth of hole doped Ba122, in particular $\text{Ba}_{1-x}\text{K}_x\text{Fe}_2\text{As}_2$ thin films, was challenging due to the difficulty in controlling volatile K. In the early stage of research on Fe-based superconductors, K-doped Ba122 was fabricated by solid-phase epitaxy [75]. Although the film showed a T_c of around 40 K, the films were only c -axis fiber textured. Almost at the same time, such films with different K contents were also grown by MBE [76], and the phase diagram (i.e. superconducting dome) was constructed. However, in-plane alignment was not reported, and hence grain boundary effects potentially masked intrinsic and pinning-related properties.

In 2014, the end member KFe_2As_2 (K122) was fabricated via solid-phase epitaxy [20]. The film grown on LSAT was weakly textured. Later, the growth conditions were optimized, resulting in epitaxial K122 thin films [21]. Briefly, a K-rich K122 polycrystalline bulk was ablated by a KrF laser (248 nm) at room temperature. The amorphous precursor film was covered by MgO substrate, and placed on an Al_2O_3 boat, which was filled with K122 powder. The whole arrangement was covered with an Al_2O_3 lid and sealed in an Ar-filled stainless tube. Finally, the sample was heat-treated at 1000 °C for 30 min. Although the film grew epitaxially on MgO with a small full width at half maximum of 0.06° for the rocking curve (the out-of-plane, 002 reflection), the film was extremely sensitive against ambient air. Hence, such films have to be protected against air during characterization.

Finally, epitaxial K-doped Ba122 thin films were realized by MBE in 2021 [22]. The key to success was to employ a low-temperature growth and fluoride substrates. The film showed a surprisingly high J_c of over 14 MA cm^{-2} at 5 K [23]. Additionally, the pinning force density of the film was higher than that of the pinning-enhanced K-doped single crystal. In the following sub-section, we review the growth of epitaxial K-doped Ba122 together with recent activities.

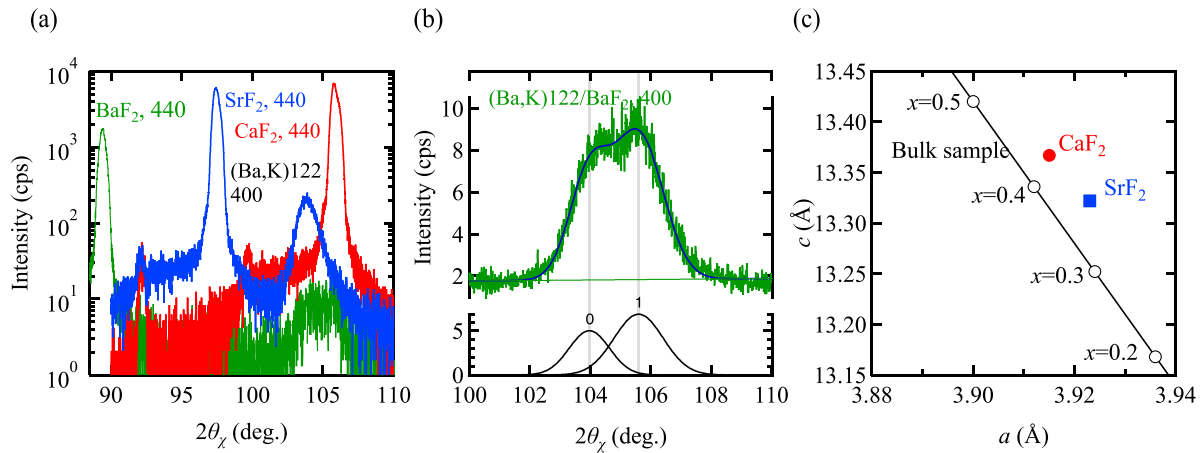


Figure 7. (a) The $2\theta_x/\phi$ -scans around the 400 reflections for K-doped Ba122 grown on AeF_2 ($Ae = Ca, Sr, \text{ and } Ba$). (b) Enlarged view of the $2\theta_x/\phi$ -scans around the 400 reflection for K-doped Ba122 grown on BaF_2 . The deconvoluted spectrum is shown. (c) The relationship between the a - and c -axis length for K-doped Ba122 thin films grown on AeF_2 substrates. The data of bulk samples ($Ba_{1-x}K_xFe_2As_2$) together with the nominal K content are also superimposed [77].

4.2. Growth methods

As stated above, a low deposition temperature of around 400°C and using fluoride substrates are important for the epitaxial growth of K-doped Ba122 [22]. Ba was charged in a W-basket, whereas Fe was placed on an Al-coated W-basket due to the high reactivity between W and Fe. In-K alloy was used as K source for safety issue as well as good controllability. Both In-K and As were charged in homemade-effusion cells. An AeF_2 (Ae : Ca, Sr and Ba) substrate cleaned by acetone was transferred into a custom-designed MBE chamber (base pressure $\sim 1.3 \times 10^{-7}$ Pa) equipped with atomic absorption spectroscopy (AAS) and electron impact emission spectroscopy (EIES). The signals obtained by AAS and EIES were fed back to a personal computer that controls resistive heaters of each element (K, Ba, and Fe). The substrate temperature was increased to around 600°C for thermal cleaning. Then the substrate was cooled to around 400°C and held at this temperature for deposition of K-doped Ba122. A 10 min growth time results in an approximate 100 nm layer thickness. K-doped Ba122 thin films were grown epitaxially and phase-pure on AeF_2 regardless of Ae [22], although the lattice mismatch of 10.8% between $Ba_{0.6}K_{0.4}Fe_2As_2$ and BaF_2 is relatively large compared with CaF_2 (−1.2%) and SrF_2 (4.6%).

Figure 7(a) shows the $2\theta_x/\phi$ -scans in the vicinity of the 400 reflections of K-doped Ba122 grown on AeF_2 . Since the in-plane lattice parameter of K-doped Ba122 is close to the lattice constant of CaF_2 divided by $\sqrt{2}$ (i.e. $a_{CaF_2}/\sqrt{2} = 3.854 \text{ \AA}$), the 400 diffraction peak of K-doped Ba122 overlaps with the 440 peak of CaF_2 . Hence the a -axis length was determined from the 103 diffraction angle and the lattice constant c . For the film grown on SrF_2 , the lattice constant a was determined from the Nelson-Riley function using the 200, 400, 220 and 440 reflections. For the film grown on BaF_2 , the peak was quite broad due to the two peaks (figure 7(b)), arising from different strain states or different doping levels. The relationship between the a - and c -axis length for K-doped Ba122 grown on CaF_2 and SrF_2 is shown in figure 7(c). For comparison, the data of bulk

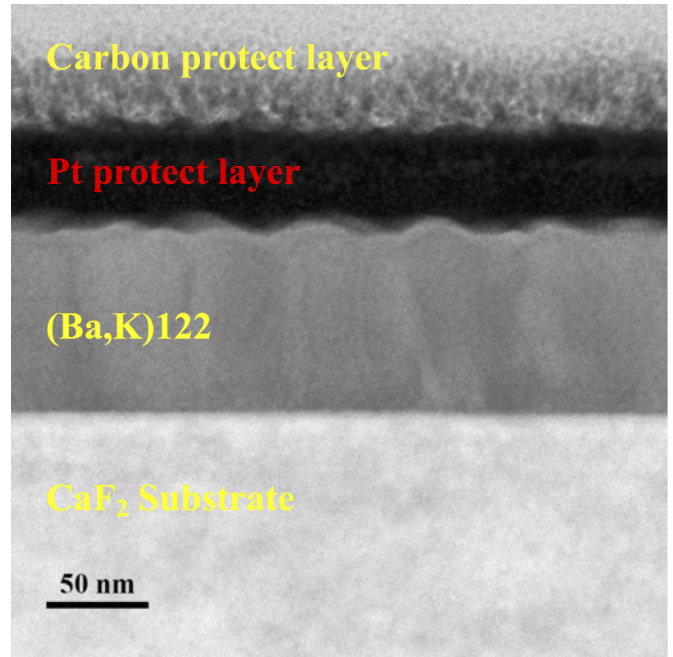


Figure 8. Bright field TEM image of the cross-sectional view for K-doped Ba122 [(Ba,K)122] on CaF_2 .

samples are also superimposed [77]. The slope of the films shifts upward from the bulk one, which may indicate that both films are strained.

Microstructural analysis shown in figure 8 revealed that the film grown on CaF_2 consisted of columnar grains having a width of $d \sim 30\text{--}60$ nm, corresponding to a matching field of ~ 2 T [23]. Additionally, the average rotation angle of the grains around the a - or b -axis is 1.5° and 1° around the c -axis. As a result, low-angle grain boundaries and their networks were present in these K-doped Ba122 films, which work as strong vortex pinning centers especially for the field direction of the substrate normal.

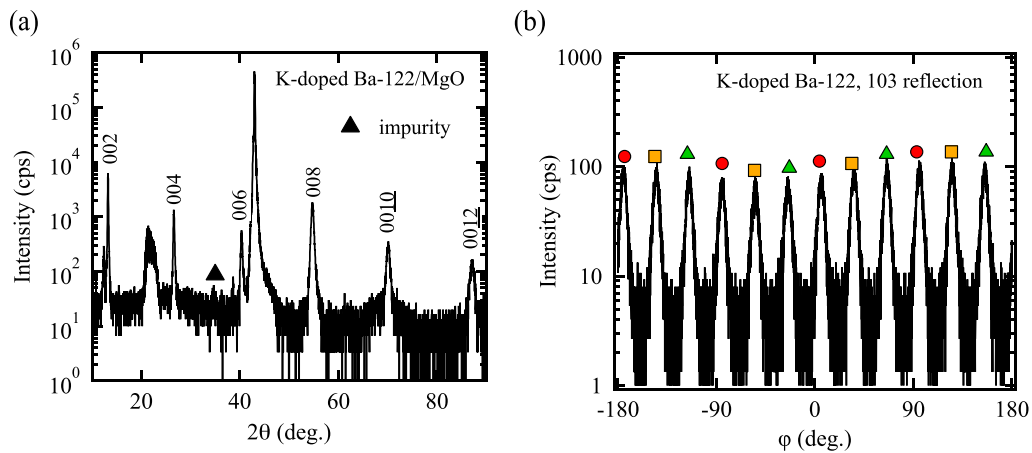


Figure 9. (a) The $2\theta/\omega$ -scan and (b) the 103 ϕ -scan for K-doped Ba122 grown on bare MgO. The peaks marked by circles, squares and triangles appeared every 30° .

Unfortunately, as fluoride bicrystal substrates have not been commercially available due to their brittle nature, it is difficult to explore grain boundary properties using bicrystal experiments. To conduct bicrystal experiments, K-doped Ba122 thin films should be realized on oxide substrates for which bicrystals are commercially available such as SrTiO₃, LSAT and MgO. Among them, MgO and SrTiO₃ have been recognized as common bicrystal substrates. For SrTiO₃, oxygen is released under ultra high vacuum conditions and, therefore, the only choice is MgO. Initially, the growth of K-doped Ba122 was attempted without buffer layer. After optimization, however, only c -axis oriented films were obtained (figure 9(a)). The 103 ϕ -scan showed that some domains were rotated around the c -axis by 30° (figure 9(b)). The reason is not clear. So far, the epitaxial growth of K-doped Ba122 has not been realized on bare MgO.

Since the growth temperature cannot be increased above 500°C due to the volatility of K, a buffer layer with good lattice matching and chemical compatibility to K-doped Ba122 is required for promoting epitaxial growth even at low temperatures. The parent Ba122 fulfills the above requirements. Additionally, undoped Ba122 has been grown epitaxially on MgO by both MBE [78] and PLD [79]. In fact, either doped or undoped Ba122 has been implemented as a buffer layer for epitaxial growth of Fe(Se,Te) [80] and SmFeAsO [81], respectively.

A 20–30 nm thick parent Ba122 buffer was grown on MgO at 720°C by MBE. Then the 100 nm thick K-doped Ba122 thin film was grown on Ba122-buffered MgO. The K content was around 40%, confirmed by TEM-EDX. The structural characterization by x-ray diffraction is summarized in figure 10. The peak splitting of the $00l$ reflections is getting obvious with higher 2θ value. The former peak corresponds to the parent (or slightly K-doped) Ba122 buffer and the latter to the actual K-doped Ba122 film. Although two phases are clearly visible in the out-of-plane scans, they are hard to recognize in in-plane scans due to the small difference in the lattice parameter

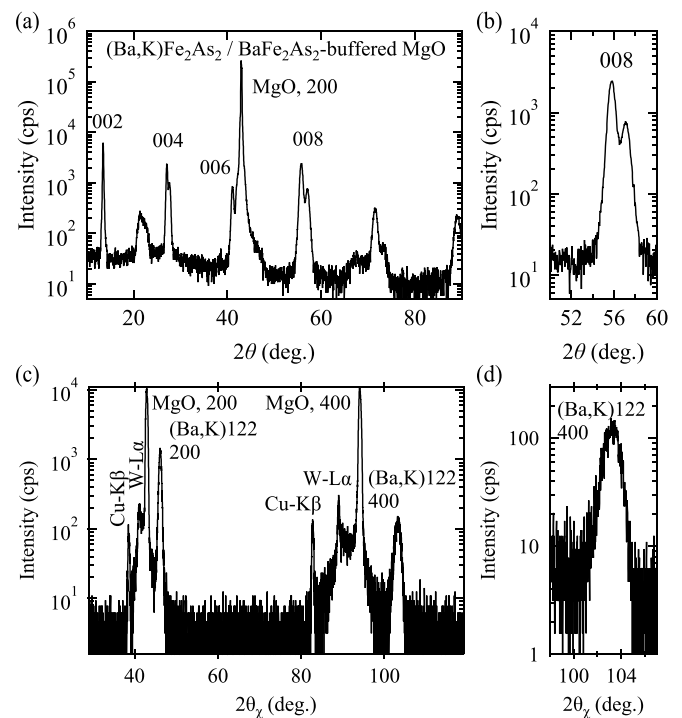


Figure 10. (a) $2\theta/\omega$ -scan and (b) enlarged view around the 008 reflection as well as (c) $2\theta_\chi/\phi$ -scan of the $h00$ reflections and (d) enlarged view around the 400 reflection for a K-doped Ba122 film grown on Ba122-buffered MgO.

a (figures 10(c) and (d)). The 103 ϕ -scan confirmed that K-doped Ba122 grew epitaxially on Ba122-buffered MgO [24].

4.3. Physical properties of $\text{Ba}_{1-x}\text{K}_x\text{Fe}_2\text{As}_2$ grown on AeF_2

As demonstrated in [22], all K-doped Ba122 films on AeF_2 had almost the same T_c of 36 ± 1 K. All films were deposited at the same growth run. Hence, the K content of all these films

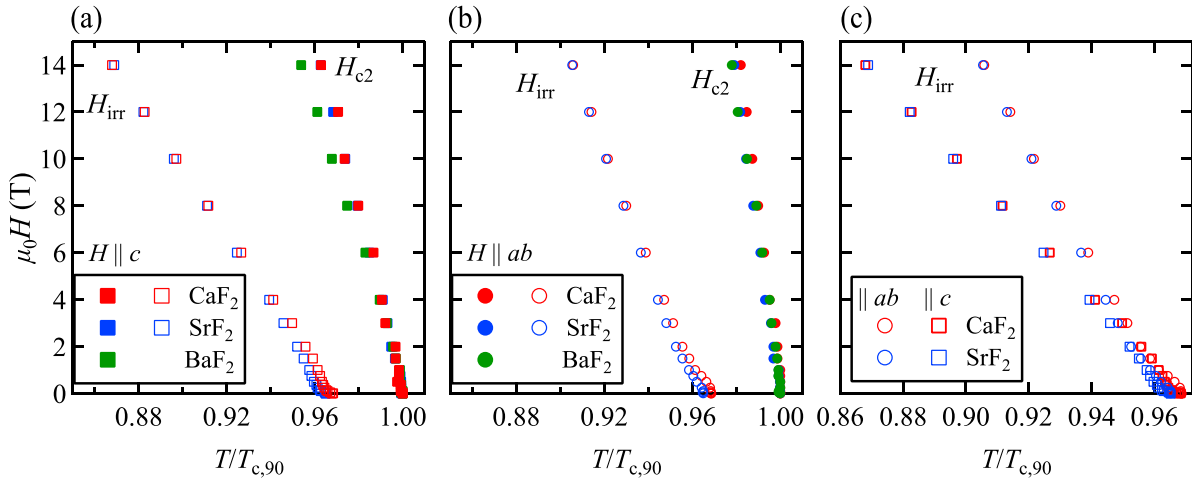


Figure 11. The upper critical field H_{c2} and the irreversibility field H_{irr} of K-doped Ba122 for (a) $H \parallel c$ and (b) $H \parallel ab$. (c) Comparison of H_{irr} between the films grown on CaF_2 and SrF_2 for both major crystallographic directions.

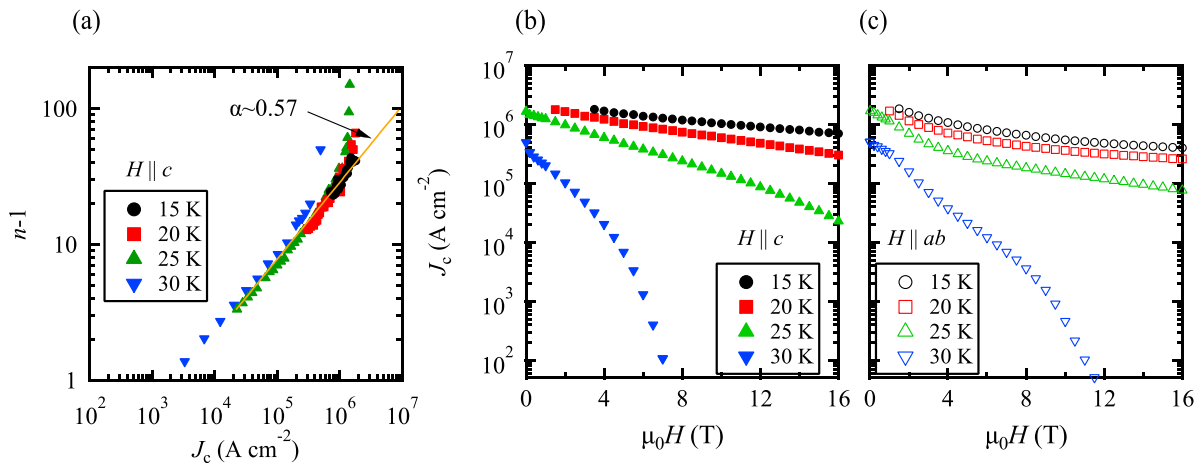


Figure 12. (a) The exponent $n - 1$ as a function of J_c for $H \parallel c$. (b) The field dependence of J_c for K-doped Ba122 grown on CaF_2 measured at various temperatures for $H \parallel c$ and (c) $H \parallel ab$. Panels (b) and (c) reproduced from [23]. CC BY 4.0.

is expected to be the same. Figure 11 shows the upper critical field H_{c2} and the irreversibility field H_{irr} as a function of reduced temperature $t = T/T_{c,90}$. For both directions, $H_{c2}(t)$ of the film grown on BaF_2 was slightly lower. This may be due to some sample degradation. In fact, H_{irr} for the film on BaF_2 was not determined. For the films on CaF_2 and SrF_2 , $H_{c2}(t)$ was almost identical, while H_{irr} of the film on CaF_2 was slightly higher at low fields. A clear kink in $H_{irr}(t)$ at around 2 T was recognized, which is ascribed to the matching field effect [23].

The critical current density J_c was determined by I - V measurements using an electrical field criterion of $1 \mu\text{Vcm}^{-1}$. The I - V characteristics can be described by $V \sim I^n$ in the vicinity of J_c , if the measured samples are free from weak-links. Here, the exponent n contains information on the pinning potential, if the measured sample is sufficiently homogenous. In fact, the field dependence of n behaves similar to that of J_c (i.e. n scales with J_c) for K-doped Ba122. This relation was reported for many superconductors, e.g. YBCO [82], $\text{LnFeAs}(\text{O},\text{F})$

[83, 84], $\text{Fe}(\text{Se},\text{Te})$ [85] and MgB_2 [86]. The following relation $n - 1 \sim J_c^\alpha$ for K-doped Ba122 was observed (figure 12(a)) with $\alpha = 0.57$. Here, we plot $n - 1$ versus J_c rather than n versus J_c , since the inverse of $n - 1$ corresponds to the flux creep rate S . Although the physical meaning of α is not fully clear, it may be related to the shape of the I - V curves near the glass-liquid transition. The data above $n > 50$ start to deviate from the trendline, which may be due to heating of the contact pads/wires. Another distinct feature compared with other Fe-based superconductors are relatively high n values, indicative of a low flux creep rate S . For instance, $n > 20$ for entire magnetic fields (up to 16 T) even at 15 K was recorded. This value is comparable to $\text{NdFeAs}(\text{O},\text{F})$ with $T_c = 47.1$ K measured at 4.2 K [84].

J_c for $H \parallel c$ is getting larger than that for $H \parallel ab$ at $T \leq 25$ K for fields sufficiently smaller than H_{irr} , which is the opposite expected from the H_{c2} anisotropy (figures 12(b) and (c)). To understand the origin of this behavior, angular dependence

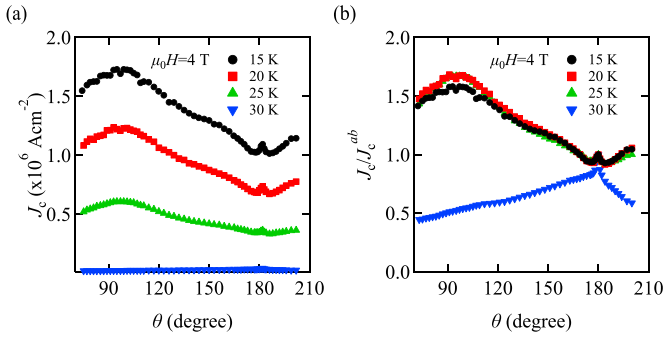


Figure 13. Angle dependence of J_c measured at 4 T and several temperatures. The respective angles $\theta = 90^\circ$ and 180° are for $H \parallel c$ and $\parallel ab$. (a) Absolute values and (b) normalized to the J_c values at $H \parallel ab$ (J_c^{ab}). Reproduced from [23]. CC BY 4.0.

of J_c was shown in figures 13(a) and (b). As can be seen in figure 13(a), J_c for $H \parallel c$ was larger than that for $H \parallel ab$ below 25 K, which is due to the presence of strong pinning along the c -axis. This is clearly seen in the normalized data (figure 13(b)). These results indicate that the pinning along the c -axis begins to be active between 30 and 25 K. The microstructure analyses revealed that grain boundaries between columnar grains of K-doped Ba122 created the c -axis correlated pinning [23].

The I - V measurements were limited at low temperatures and fields due to heating at the contact pads/wires. Therefore, the field dependence of J_c for $H \parallel c$ was evaluated from magnetization measurements too (figures 14(a) and (b)). A large self-field J_c of 14.4 MA cm^{-2} was recorded at 4 K. Self-field J_c scales with $[1 - (T/T_c)^2]^m$ with $m = 1.93$, as shown in figure 14(c). Theoretically, $m = 7/6$ and $5/2$ represent the δT_c -pinning and δl -pinning, respectively [88]. The intermediate value obtained for this film indicates mixed pinning, despite insufficient data close to T_c .

Figure 14(d) shows the field dependence of the pinning force density F_p for the K-doped Ba122 thin film on CaF_2 obtained from J_c in figure 14(b). As can be seen, F_p of the K-doped Ba122 thin film is higher than that of a Pb-ion irradiated single crystal up to 4 T [87]. These results suggest that low angle grain boundaries and their networks act as strong pinning centers, comparable to the pinning enhancement achieved by ion-irradiation.

4.4. Physical properties of $\text{Ba}_{1-x}\text{K}_x\text{Fe}_2\text{As}_2$ grown on MgO

The temperature dependence of the resistivity of K-doped Ba122 on bare MgO shown in figure 9(a) exhibited a low $T_{c,90}$ of 33.2 K (figure 15(a)). Due to the presence of high angle grain boundaries, a large transition width of $T_{c,90} - T_{c,0} = 3.2 \text{ K}$ was observed. The broadening of the superconducting transition was more obvious with fields (figure 15(b)). Once the high angle grain boundaries are eliminated, such broadening is absent: figures 15(c) and (d) show the temperature dependence of the resistance for the K-doped Ba122 epitaxial film grown on Ba122-buffered MgO. The film

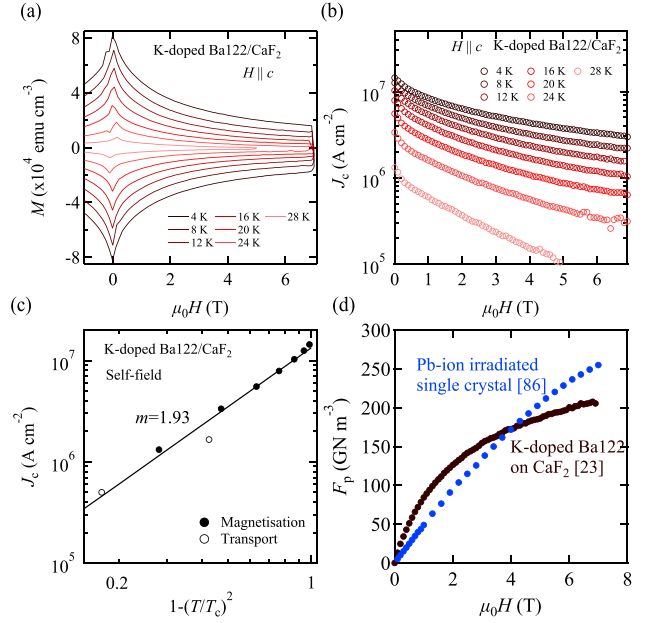


Figure 14. (a) Field dependence of magnetization M measured at various temperatures. The applied magnetic field was $H \parallel c$. (b) Field dependence of J_c extracted from the M - H measurement shown in (a). (c) Self-field J_c as a function of $1 - (T/T_c)^2$. (d) Field dependence of pinning force density F_p for $H \parallel c$ at 4 K. For comparison, the data of Pb-ion-irradiated K-doped Ba122 single crystal measured at 5 K are also shown [87]. Panels (a), (b) and (d) reproduced from [23]. CC BY 4.0.

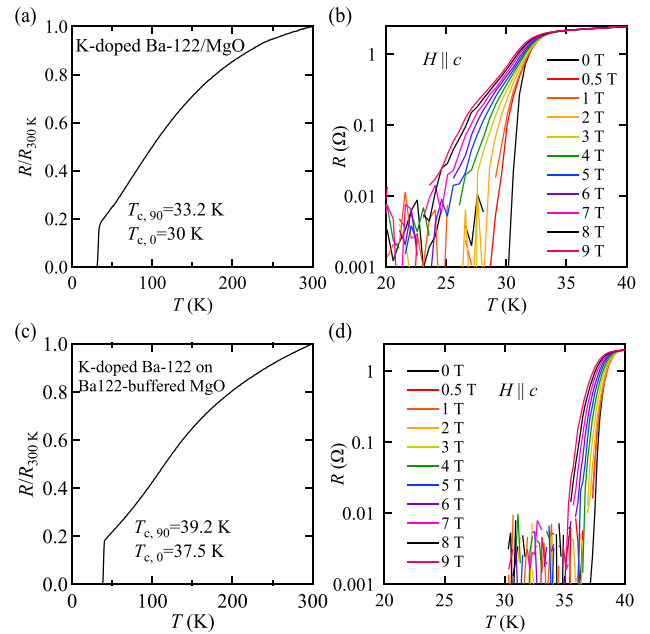


Figure 15. Comparison of the resistive transition in zero field and for $H \parallel c$ between K-doped Ba122 film on bare MgO (a), (b) and on Ba122-buffered MgO (c), (d).

showed a high $T_{c,90}$ of 39.2 K with a small transition width of 1.7 K. The high T_c value is ascribed to the strain effect [24].

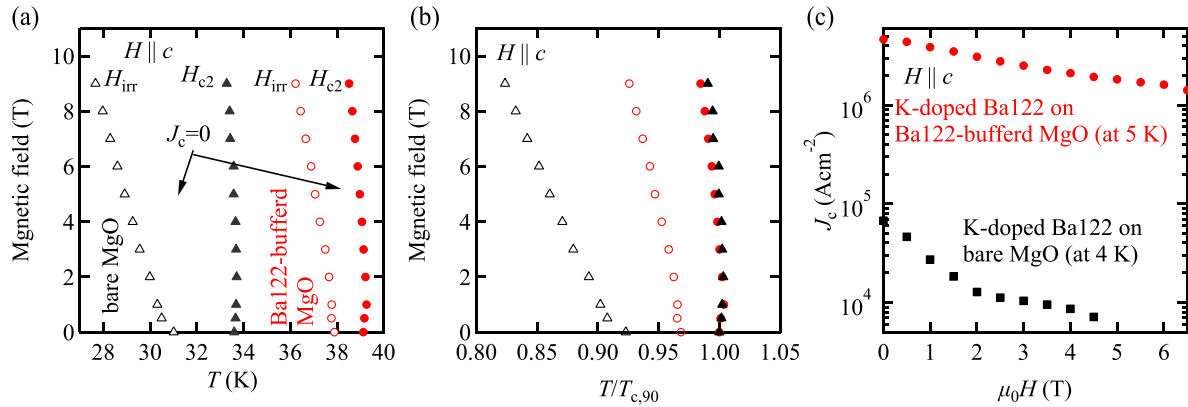


Figure 16. (a) Magnetic phase diagram for K-doped Ba122 grown on bare MgO (black) and Ba122-buffered MgO (red) for $H \parallel c$. The solid and open symbols represent the upper critical field H_{c2} and the irreversibility field H_{irr} , respectively. (b) The phase diagram shown in (a) is re-plotted as a function of reduced temperature. (c) Field dependence of J_c for K-doped Ba122 grown on Ba122-buffered MgO (circle) and bare MgO (square). Applied magnetic field was parallel to the c -axis.

The magnetic phase diagrams extracted from figure 15 are shown in figures 16(a) and (b). Due to the presence of high angle grain boundaries for the film grown on bare MgO, the region of reversible vortex motion (and hence zero J_c) is larger compared with the film on Ba122-buffered MgO. It can be seen from figure 16(b) that the upper critical field for both films are almost comparable, if the data are plotted as a function of reduced temperature.

The presence of high angle grain boundaries also reduces J_c significantly (figure 16(c)). Here, J_c was obtained from the $M-H$ measurements using the Bean model. As can be seen, the self-field J_c of the film grown on bare MgO is two orders of magnitude lower than on Ba122-buffered MgO. Additionally, J_c decreased quickly with H for the film on bare MgO.

5. Discussion and summary

Table 2 summarizes the deposition methods, substrates, the maximum T_c and the maximum self-field J_c for the various Fe-based superconductors reviewed in this article. Self-field J_c of (Li,Fe)OHFeSe was estimated by an extrapolation to 4 K. Except for $\text{SmFe}_{1-x}\text{Co}_x\text{AsO}$ with significantly lower T_c , self-field J_c of (Li,Fe)OHFeSe, NdFeAs(O,H), and $\text{Ba}_{1-x}\text{K}_x\text{Fe}_2\text{As}_2$ is more than 10 MA cm^{-2} at low temperatures (i.e. below 5 K). Although self-field J_c of Mn-doped (Li,Fe)OHFeSe has not been reported, in-field J_c is relatively high (i.e. 0.32 MA cm^{-2} at 33 T and 5 K for $H \parallel c$, figure 17) due to the pinning induced by Mn. J_c of SmFeAs(O,H) is one order of magnitude lower than that of NdFeAs(O,H). The reason for the low J_c is not clear yet. The highest self-field J_c was obtained for NdFeAs(O,H), followed by pristine (Li,Fe)OHFeSe.

Figure 17(a) summarizes the in-field J_c for various Fe-based superconductors shown in table 2. For comparison, the

data of other Fe-based superconductors grown on single crystalline substrates are superimposed. Because of the clean film of (Li,Fe)OHFeSe, J_c decreased very quickly with fields. But the pinning-enhanced Mn-doped (Li,Fe)OHFeSe was superior to other Fe-based superconductors, especially at high fields. This is also clearly seen in the field dependence of pinning force density F_p (figure 17(b)). Decrease of J_c in low-field regime was significant for the microstructurally clean NdFeAs(O,H), NdFeAs(O,F) and P-doped Ba122. films. A high F_p of over 200 GNm^{-3} was recorded for K-doped Ba122 due to the highly c -axis-correlated grain-boundaries. This value is almost the same as for a Pb-ion irradiated K-doped Ba122 single crystal [87].

Although the main crystal classes and many of the different Fe-based superconductors have been fabricated in the form of epitaxial thin films, several compounds such as $\text{Ca}_{1-x}\text{La}_x\text{FeAs}_2$ (112) [92] and $\text{CaAFe}_4\text{As}_4$ ($A = \text{K, Rb, Cs}$) (1144) [93] as well as structures with large blocking layers have not yet been realized as thin films. Fabricating such compounds is challenging due to the presence of volatile elements; and so far, no reports on the attempt on the growth of those films have been published. This should be a focus of future studies.

Hydrogen-doped LnFeAsO is a good model system for increasing the depairing current density J_d by a heavy doping method. Unlike cuprates, the superconducting transition temperature of LnFeAs(O,H) stays constant around 50 K over a wide range of doping. If the condensation energy is increased by over-doping, J_d and, hence, J_c can be increased. Systematic investigation is necessary to prove this scenario.

As stated above, realizing epitaxial thin films gives an opportunity for studying the nature of grain boundaries. In fact, we have studied the grain boundary characteristics of K-doped Ba122 [94, 95], which will be published in near future.

Table 2. The list of Fe-based superconductors reviewed in this article. Growth method, substrates, and their physical parameters are summarized. Self-field J_c for $\text{SmFeAsO}_{1-x}\text{H}_x$ at 5 K and $\text{Ba}_{1-x}\text{K}_x\text{Fe}_2\text{As}_2$ at 4 K was evaluated by a magnetization method. For $\text{NdFeAsO}_{1-x}\text{H}_x$ transport measurements were employed for self-field J_c at 4 K.

Chemical formula	Deposition method	Substrate	Max. T_c	Self-field J_c
(Li,Fe)OHFeSe	MHE	LaAlO ₃	42 K	11 MA cm ⁻² (4 K)
Mn-doped (Li,Fe)OHFeSe	MHE	LaAlO ₃	36 K	N. A.
SmFeAsO _{1-x} H _x	PLD	MgO	48 K	2 MA cm ⁻² (5 K)
SmFe _{1-x} Co _x AsO	PLD	CaF ₂ , MgO, LaAlO ₃	17 K	N. A.
NdFeAsO _{1-x} H _x	MBE	MgO	46 K	17 MA cm ⁻² (4 K)
Ba _{1-x} K _x Fe ₂ As ₂	MBE	AeF ₂ , MgO	39.8 K	14.4 MA cm ⁻² (4 K)

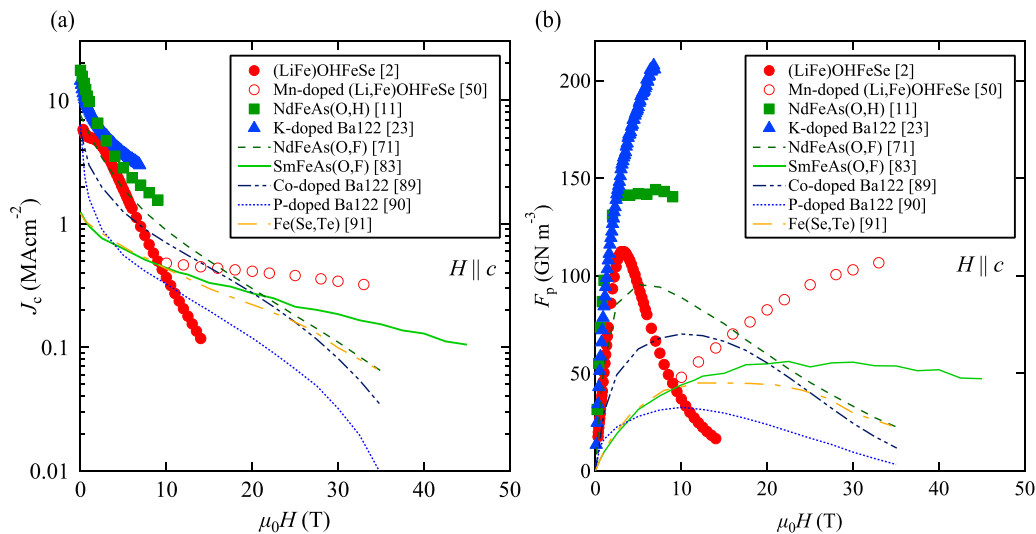


Figure 17. (a) $J_c - H$ properties of various Fe-based superconductors shown in table 2 measured at low temperatures. Magnetic field was applied parallel to the c -axis. The data of NdFeAs(O,F) grown on MgO [71], SmFeAs(O,F) grown on CaF₂ [83], Co-doped Ba122 grown on CaF₂ [89], P-doped Ba122 grown on MgO [90] and Fe(Se,Te) grown on SrTiO₃ with CeO₂ buffer [91] are plotted for comparison. (b) Corresponding $F_p - H$.

Data availability statement

All data that support the findings of this study are included within the article (and any supplementary files).

Acknowledgments

The authors thank Dongyi Qin, Michio Naito, Zimeng Guo, Hongy Gao, Takafumi Hatano, Hiroshi Ikuta, Dong Li, and Xiaoli Dong. This work was supported by JST CREST Grant Number JPMJCR18J4, JSPS Grant-in-Aid for Scientific Research (B) Grant Number 20H02681, Japan-German Research Cooperative Program between JSPS and DAAD, Grant Number JPJSBP120203506, and DFG Project HA 6407/4-1.

ORCID iDs

Kazumasa Iida <https://orcid.org/0000-0003-1038-9630>
 Jens Hänisch <https://orcid.org/0000-0003-2757-236X>
 Akiyasu Yamamoto <https://orcid.org/0000-0001-6346-3422>

References

- [1] Huang Y L *et al* 2017 Matrix-assisted fabrication and exotic charge mobility of (Li, Fe)OHFeSe superconductor films (arXiv:1711.02920)
- [2] Hänisch J, Huang Y, Li D, Yuan J, Jin K, Dong X, Talantsev E, Holzapfel B and Zhao Z 2020 *Supercond. Sci. Technol.* **33** 114009
- [3] Dong X *et al* 2015 *Phys. Rev. B* **92** 064515
- [4] Wang C, Yi X, Qiu Y, Tang Q, Zhang X, Zhang X, Luo Y, Yu B 2016 *Supercond. Sci. Technol.* **29** 055003
- [5] Zhao L *et al* 2016 *Nat. Commun.* **7** 10608
- [6] Zhang G Y, Chou M and Lin C T 2017 *Crystals* **7** 167
- [7] Sun Y, Pyon S, Yang R, Qiu X, Feng J, Shi Z and Tamegai T 2019 *J. Phys. Soc. Japan* **88** 034703
- [8] Matsumoto J, Hanzawa K, Sasase M, Haindl S, Katase T, Hiramatsu H and Hosono H 2019 *Phys. Rev. Mater.* **3** 103401
- [9] Hiramatsu H, Matsumoto J and Hosono H 2020 *Appl. Phys. Express* **13** 073002
- [10] Hanzawa K, Matsumoto J, Iimura S, Kohama Y, Hiramatsu H and Hosono H 2022 *Phys. Rev. Mater.* **6** L111801
- [11] Kondo K, Motoki S, Hatano T, Urata T, Iida K and Ikuta H 2020 *Supercond. Sci. Technol.* **33** 09LT01
- [12] Iida K, Hänisch J, Kondo K, Chen M, Hatano T, Wang C, Saito H, Hata S and Ikuta H 2021 *Sci. Rep.* **11** 5636

- [13] Chen M Y, Iida K, Kondo K, Hänisch J, Hatano T and Ikuta H 2022 *Phys. Rev. Mater.* **6** 054802
- [14] Imura S, Muramoto T, Fujitsu S, Matsuishi S and Hosono H 2017 *J. Asian Ceram. Soc.* **5** 357
- [15] Haindl S, Sato M, Wurmehl S, Büchner B and Kampert E 2020 *Supercond. Sci. Technol.* **33** 105004
- [16] Haindl S, Nikolaev S, Sato M, Sasase M and Maclaren I 2021 *NPG Asia Mater.* **13** 67
- [17] Zhigadlo N D, Weyeneth S, Katrych S, Moll P J W, Rogacki K, Bosma S, Puzniak R, Karpinski J and Batlogg B 2012 *Phys. Rev. B* **86** 214509
- [18] Hong X *et al* 2020 *Phys. Rev. Lett.* **125** 067001
- [19] Scaravaggi F *et al* 2021 *Phys. Rev. B* **103** 174506
- [20] Hiramatsu H, Matsuda S, Sato H, Kamiya T and Hosono H 2014 *Appl. Mater. Interfaces* **6** 14293
- [21] Hatakeyama T, Sato H, Hiramatsu H, Kamiya T and Hosono H 2016 *Appl. Phys. Express* **9** 055505
- [22] Qin D, Iida K, Hatano T, Saito H, Ma Y, Wang C, Hata S, Naito M and Yamamoto A 2021 *Phys. Rev. Mater.* **5** 014801
- [23] Iida K *et al* 2021 *NPG Asia Mater.* **13** 68
- [24] Qin D, Iida K, Guo Z, Wang C, Saito H, Hata S, Naito M and Yamamoto A 2022 *Supercond. Sci. Technol.* **35** 09LT01
- [25] Luo H, Wang Z, Yang H, Cheng P, Zhu X and Wen H 2008 *Supercond. Sci. Technol.* **21** 125014
- [26] Guo Z, Sun F and Yuan W 2017 *Cryst. Growth Des.* **17** 2238
- [27] Vivanco H K and Rodriguez E E 2016 *J. Solid State Chem.* **242** 3
- [28] Dong X, Zhou F and Zhao Z 2020 *Front. Phys.* **8** 586182
- [29] Burrard-Lucas M *et al* 2013 *Nat. Mater.* **12** 15
- [30] Gao Z, Zeng S, Zhu B, Li B, Hao Q, Hu Y, Wang D and Tang K 2018 *Sci. China Mater.* **61** 977
- [31] Shi M Z *et al* 2018 *New J. Phys.* **20** 123007
- [32] Shi M Z, Wang N Z, Lei B, Shang C, Meng F B, Ma L K, Zhang F X, Kuang D Z and Chen X H 2018 *Phys. Rev. Mater.* **2** 074801
- [33] Rendenbach B, Hohl T, Harm S, Hoch C and Johrendt D 2021 *J. Am. Chem. Soc.* **143** 3043
- [34] Lu X F *et al* 2015 *Nat. Mater.* **14** 325
- [35] Zhou X, Eckberg C, Wilfong B, Liou S-C, Vivanco H K, Paglionebc J and Rodriguez E E 2017 *Chem. Sci.* **8** 3781
- [36] Lu X F, Wang N Z, Zhang G H, Luo X G, Ma Z M, Lei B, Huang F Q and Chen X H 2014 *Phys. Rev. B* **89** 020507
- [37] Deng L *et al* 2021 *Proc. Natl Acad. Sci. USA* **118** e2108938118
- [38] Shiogai J, Kimura S, Awaji S, Nojima T and Tsukazaki A 2018 *Phys. Rev. B* **97** 174520
- [39] Amrein T, Schultz L, Kabius B and Urban K 1995 *Phys. Rev. B* **51** 6792
- [40] Urban C, Valmianski I, Pachmayr U, Basaran A C, Johrendt D and Schuller I K 2018 *Phys. Rev. B* **97** 024516
- [41] Sun J P *et al* 2018 *Nat. Commun.* **9** 380
- [42] Liu Q *et al* 2018 *Phys. Rev. X* **8** 041056
- [43] Li D, Shen P, Ma S, Wei Z, Yuan J, Jin K, Yu L, Zhou F, Dong X and Zhao Z 2021 *Chin. Phys. B* **30** 017402
- [44] Li D *et al* 2022 *Supercond. Sci. Technol.* **35** 064007
- [45] Huang Y *et al* 2022 *Chin. Phys. Lett.* **34** 077404
- [46] Talantsev E F and Tallon J L 2015 *Nat. Commun.* **6** 7820
- [47] Wilfong B, Zhou X, Zheng H, Babra N, Brown C M, Lynn J W, Taddei K M, Paglione J and Rodriguez E E 2020 *Phys. Rev. Mater.* **4** 034803
- [48] Yadav A K, Sanchela A V, Thakur A D and Tomya C 2015 *Solid State Commun.* **202** 8
- [49] Luo S, Wu Y, Wen Z, Cui Y, Zhao Y and Chen Y 2022 *J. Supercond. Nov. Magn.* **35** 2319–25
- [50] Li D *et al* 2019 *Supercond. Sci. Technol.* **32** 12LT01
- [51] Li D *et al* 2022 *Chin. Phys. Lett.* **39** 127402
- [52] He G, Li D, Jost D, Baum A, Shen P P, Dong X L, Zhao Z X and Hackl R 2020 *Phys. Rev. Lett.* **125** 217002
- [53] Kappenberger R, Aswartham S, Scaravaggi F, Blum C, Sturza M, Wolter A, Wurmehl S and Büchner B 2018 *J. Cryst. Growth* **483** 9
- [54] Hiramatsu H, Katase T, Kamiya T, Hirano M and Hosono H 2008 *Appl. Phys. Lett.* **93** 162504
- [55] Kidszun M, Haindl S, Reich E, Hänisch J, Iida K, Schultz L and Holzapfel B 2009 *Supercond. Sci. Technol.* **23** 022002
- [56] Kawaguchi T, Uemura H, Ohno T, Tabuchi M, Ujihara T, Takenaka K, Takeda Y and Ikuta H 2010 *Appl. Phys. Lett.* **97** 042509
- [57] Ueda S, Takeda S, Takano S, Yamamoto A and Naito M 2011 *Appl. Phys. Lett.* **99** 232505
- [58] Backen E, Haindl S, Niemeier T, Hühne R, Freudenberger T, Werner J, Behr G, Schultz L and Holzapfel B 2008 *Supercond. Sci. Technol.* **21** 122001
- [59] Kidszun M, Haindl S, Thersleff T, Hänisch J, Kauffmann A, Iida K, Freudenberger J, Schultz L and Holzapfel B 2011 *Phys. Rev. Lett.* **106** 137001
- [60] Kawaguchi T, Uemura H, Ohno T, Watanabe R, Tabuchi M, Ujihara T, Takenaka K, Takeda Y and Ikuta H 2009 *Appl. Phys. Express* **2** 093002
- [61] Haindl S, Kinjo H, Hanzawa K, Hiramatsu H and Hosono H 2018 *Appl. Surf. Sci.* **437** 418
- [62] Sugawara H, Tsuneki T, Watanabe D, Yamamoto A, Sakoda M and Naito M 2015 *Supercond. Sci. Technol.* **28** 015005
- [63] Chihara M, Sumiya N, Arai K, Ichinose A, Tsukada I, Hatano T, Iida K and Ikuta H 2015 *Physica C* **518** 69
- [64] Sakoda M, Ishii A, Takinaka K and Naito M 2017 *J. Appl. Phys.* **122** 015306
- [65] Fujioka M *et al* 2013 *Supercond. Sci. Technol.* **26** 085023
- [66] Imura S, Okanishi H, Matsuishi S, Hiraka H, Honda T, Ikeda K, Hansen T C, Otomo T and Hosono H 2017 *Proc. Natl Acad. Sci. USA* **114** E4354
- [67] Uemura H, Kawaguchi T, Ohno T, Tabuchi M, Ujihara T, Takeda Y and Ikuta H 2012 *Solid State Commun.* **152** 735
- [68] Iida K *et al* 2014 *Appl. Phys. Lett.* **105** 172602
- [69] Guo Z, Gao H, Kondo K, Hatano T, Iida K, Hänisch J, Ikuta H and Hata S 2021 *ACS Appl. Electron. Mater.* **3** 3158
- [70] Muraba Y, Matsuishi S and Hosono H 2014 *Phys. Rev. B* **89** 094501
- [71] Weiss-Kauffmann S *et al* 2019 *Nanoscale Adv.* **1** 3036
- [72] Tinkham M 1975 *Introduction to Superconductivity* (New York: McGraw-Hill)
- [73] Stangl A, Palau A, Deutscher G, Obradors X and Puig T 2021 *Sci. Rep.* **11** 8176
- [74] Miura M *et al* 2022 *NPG Asia Mater.* **14** 85
- [75] Lee N H, Jung S-G, Kim D H and Kang W N 2010 *Appl. Phys. Lett.* **96** 202505
- [76] Yamagishi T, Ueda S, Takeda S, Takano S, Mitsuda A and Naito M 2011 *Physica C* **471** 1177
- [77] Rotther M, Pangerl M, Tegel M and Johrendt D 2008 *Angew. Chem., Int. Ed.* **47** 7949
- [78] Kawaguchi T, Sakagami A, Mori Y, Tabuchi M, Ujihara T, Takeda Y and Ikuta H 2014 *Supercond. Sci. Technol.* **27** 065005
- [79] Engelmann J *et al* 2013 *Nat. Commun.* **4** 2877
- [80] Sakoda M, Iida K and Naito M 2018 *Supercond. Sci. Technol.* **31** 093001
- [81] Haindl S, Hanzawa K, Sato H, Hiramatsu H and Hosono H 2016 *Sci. Rep.* **6** 14293
- [82] Opherden L *et al* 2016 *Sci. Rep.* **6** 21188
- [83] Iida K *et al* 2013 *Sci. Rep.* **3** 2139
- [84] Tarantini C *et al* 2016 *Sci. Rep.* **6** 36047
- [85] Iida K *et al* 2013 *Phys. Rev. B* **87** 104510
- [86] Kim J H, Dou S X, Matsumoto A, Choi S, Kiyoshi T and Kumakura H 2010 *Physica C* **470** 1207

- [87] Fang L *et al* 2012 *Appl. Phys. Lett.* **101** 012601
- [88] Ijaduola A O, Thompson J R, Feenstra R, Christen D K, Gapuda A and Song X 2006 *Phys. Rev. B* **73** 134502
- [89] Tarantini C, Kametani F, Lee S, Jiang J, Weiss J D, Jaroszynski J, Hellstrom E E, Eom C B and Larbalestier D C 2014 *Sci. Rep.* **4** 7305
- [90] Kurth F *et al* 2015 *Appl. Phys. Lett.* **106** 072602
- [91] Si W, Han S J, Shi X, Ehrlich S N, Jaroszynski J, Goyal A and Li Q 2013 *Nat. Commun.* **4** 1347
- [92] Katayama N *et al* 2013 *J. Phys. Soc. Japan* **82** 123702
- [93] Iyo A, Kawashima K, Kinjo T, Nishio T, Ishida S, Fujihisa H, Gotoh Y, Kihou K, Eisaki H and Yoshida Y 2016 *J. Am. Chem. Soc.* **138** 3410
- [94] Hatano T, Qin D, Iida K, Saito H, Guo Z, Gao H, Hata S, Naito M and Yamamoto A 2021 Critical current properties of artificial grain boundaries of K-doped BaFe₂As₂ realization on MgO bicrystal substrates *Materials Research Meeting (Yokohama, Japan)*
- [95] Iida K, Qin D, Hatano T, Gao H, Guo Z, Wang C, Saito H, Hata S, Naito M and Yamamoto A 2022 *Materials Research Society MRS Spring Meeting & Exhibit (Virtual)*